Check for updates

Role of defects on TiO$_2$/SiO$_2$ composites for boosting photocatalytic water splitting

Wibawa Hendra Saputera, [iD] * Jenny Rizkiana, Winny Wulandari and Dwiwahju Sasongko

Defect engineering of semiconductor photocatalysts is considered as an evolving strategy to adjust their physiochemical properties and boost photoreactivity of the materials. Here, hydrogenation and UV light pre-treatment of TiO$_2$/SiO$_2$ composite with the ratio of 9 : 1 (9TiO$_2$/1SiO$_2$) were conducted to generate Ti^{3+} and non-bridging oxygen holes center (NBOHC) defects, respectively. The 9TiO$_2$/1SiO$_2$ composite exhibited much higher photocatalytic water splitting than neat TiO$_2$ and SiO$_2$ as a consequence of the electronic structure effects induced by the defect sites. Electron paramagnetic resonance (EPR) indicated that hydrogenated and UV light pre-treated of 9TiO$_2$/1SiO$_2$ boosted a higher density of Ti^{3+} and NBOHC defect which could serve to suppress photogenerated electron–hole pair recombination and act as shallow donors to trap photoexcited electron. Overall, both defect sites in 9TiO$_2$/1SiO$_2$ delivered advantageous characteristic relative to neat TiO$_2$ and SiO$_2$ with the finding clearly illustrating the value of defect engineering in enhancing photocatalytic performance.

Introduction

Photocatalytic water splitting into oxygen and hydrogen is possible, feasible, sustainable and a promising approach for solar energy storage and generating clean energy without any pollution.[1–3] Photocatalytic overall water splitting can occur *via* either a stepwise two-electron pathway through hydrogen peroxide generation or a one-step four-electron pathway, wherein the four-electron process for O$_2$ evolution is thermodynamically favorable compared to the two-electron process for H$_2$O$_2$ generation.[1,4] Nevertheless, the kinetically two-electron process for H$_2$O$_2$ formation is someway easier to occur. Thus, it remains a task to control the electron pathway in order to improve the energy conversion and utilization.

Several catalysts have been used for photocatalytic water splitting application, including g-C$_3$N$_4$,[5–8] BiVO$_4$,[9–11] carbon nanotubes,[12] Ag-based,[13] TiO$_2$,[14–17] *etc.* Among various catalysts, the most commonly used metal oxide based catalyst, TiO$_2$, has gained much attention due to their relatively high activity, abundant, non-toxic, and low-cost.[18] However, this photocatalyst is still far away for large-scale applications because of their low photocatalytic efficiency due to rapid recombination of photo-generated electrons and holes, the unsuitable energy band position and values, and sluggish surface reaction kinetic.[18,19] Thus, there is vital need to fabricate and design low-cost and more efficient photocatalysts.

Several strategies have been developed in order to enhance photocatalytic efficiency of TiO$_2$ based photocatalyst including formation of heterojunction with another semiconductor[20] and doping with foreign atoms.[21] Besides, defect engineering of TiO$_2$ photocatalyst is also one of the approaches commonly used to suppress electron–hole recombination by creating mid-gap states, and thus improving photocatalytic performance.[22–24] It has been reported that hydrogen reduction treatment has been successfully used to generate Ti^{3+} associated with oxygen vacancy defects.[25–27] On the other hand, SiO$_2$ is also known to possess defect sites when subject to appropriate treatment conditions. Recently, it has been reported that UV light pre-treatment has been able to generate non-bridging oxygen holes center (NBOHC, $\equiv$Si–O$^\bullet$) and capable of dehydrogenating organic compounds.[28,29] The question then arises to whether Ti^{3+} and NBOHC can be effectively generated in TiO$_2$/SiO$_2$ composites using a combined treatment strategy including thermal treatment coupled with light illumination and then harnessed to invoke synergism for photocatalytic water splitting.

The ensuing work examines the prospect of hydrogenation and UV light pre-treatment with the intent to generate multiple defects on TiO$_2$/SiO$_2$ comprising Ti^{3+} and non-bridging oxygen holes center (NBOHC) and evaluate the capacity for photocatalytic water splitting. Knowledge gained from physiochemical properties coupled with X-ray photoelectron spectroscopy (XPS) and electron paramagnetic resonance (EPR) analysis were used to identify the role of defects on TiO$_2$/SiO$_2$ for enhancing photocatalytic water splitting.

Research Group on Energy and Chemical Engineering Processing System, Department of Chemical Engineering, Institut Teknologi Bandung, Bandung 40132, Indonesia. E-mail: hendra@che.itb.ac.id

Experimental

Materials

Titanium isopropoxide (TTIP, Sigma-Aldrich, ≥97%) tetraethylorthosilicate (TEOS, Sigma-Aldrich, ≥98.5%), ethanol (Sigma Aldrich, >96%), HCl (Sigma Aldrich, 37%), hydrogen (AGI, >99.99%), nitrogen (AGI, >99.99%), air (AGI, Dry Compressed Air).

Methods

Catalyst synthesis. TiO$_2$, SiO$_2$, and binary 9TiO$_2$–1SiO$_2$ composites synthesized using a conventional sol–gel method. The ratio of 9 : 1 TiO$_2$/SiO$_2$ is chosen based on the reported work by Saputera *et al.*[29] which showed that 9 : 1 ratio exhibited the best catalytic performance for catalytic oxidation of organic compound. Briefly, titanium(iv) isoproxide (TTIP) and tetraethylorthosilicate (TEOS) were used as starting materials. Ethanol was used as a solvent. Firstly, TTIP was dissolved in ethanol mixed TEOS, stirred 20 min at a room temperature and followed by the addition of 1 M HCl to the solution until pH = 3.5. Distilled water was finally added and the solution was then stirred for 20 min. The solution was dried at 105 °C for 12 h. Heat treatment consisted of calcination and hydrogenation was then performed in a tubular furnace. Calcination was performed at 300 °C under a flowing air stream with heating and flow rates of 5 °C min^{-1} and 50 mL min^{-1}, respectively. The calcination conditions were maintained for 3 h. Hydrogenation was conducted at 500 °C under a 10 vol% H$_2$/N$_2$ flowing gas stream with heating and total flow rates of 5 °C min^{-1} and 50 mL min^{-1}, respectively. The hydrogenation conditions were maintained for 3 h. UV light pre-treatment was conducted at spiral reactor for 30 minutes.[30]

Catalyst characterizations. Sample morphology was investigated by high resolution transmission electron microscopy (HRTEM), using a Hitachi H9500 equipped with an energy dispersive X-ray spectroscopy (EDX) digital imaging. The particle size distribution was determined using ImageJ software by averaging 100 particles size. The crystal structure of the samples was evaluated by X-ray diffraction (XRD) using a Bruker D8 Advance. Data were collected by varying 2θ between 20° and 80° with a step size of 0.026°. UV-vis absorption spectra of the samples were acquired using a Shimadzu 2450 spectrophotometer with BaSO$_4$ as the reference.

The existence of defects was evaluated using electron paramagnetic resonance (EPR) spectroscopy (Bruker Elexys 500 model). EPR measurements were conducted at 9.419 GHz (X-band). The microwave power, the modulation amplitude, and the temperature were set at 2 mW, 5 G, and 120 K, respectively. UV light pre-treatment was performed outside the EPR cavity using a light source of 20 W black light blue lamps with a maximum emission at 365 nm.

X-ray photoelectron spectroscopy analyses were performed using a VG ESCALAB MkII spectrometer. The radiation was provided by a monochromatic X-ray source (Al Kα, 1486.6 eV) operated at a 164 W emission power. Ti 2p, Si 2p, and O 1s core-level spectra were recorded, and the corresponding binding energies were referenced to the C 1s peak at 285 eV (from surface carbon). The core-level spectra were deconvoluted into their components with a mixed line shape of Lorentzian (20%) – Gaussian (80%), using the software package Thermo Avantage after subtraction of the Shirley-type background.

Photocatalytic activity assessment. Hydrogen evolution was used as the model reaction to assess the photocatalytic performance of the catalysts. Typically, 100 mg of photocatalyst was dispersed in 150 mL of water and methanol with a volume ratio of 9 : 1 under ultra-sonication. The reaction was carried out in an enclosed top-irradiated Pyrex cell with a quartz window. Prior to light irradiation, argon gas purging was performed for 30 minutes to remove air from the reactor. The suspension was then irradiated by a 300 W xenon lamp (Toption, Top X-300) for 5 h under continuous stirring and a water jacket was placed on the top of the reactor. Hydrogen generation was analyzed and quantified every 30 minutes using a gas chromatograph equipped with a thermal conductivity detector (TCD) (Shimadzu, Argon as the carrier gas). The catalysts were collected by centrifuging and washed with water and ethanol to remove the impurities. The recovered catalysts were oven-dried at 70 °C overnight.

Results and discussion

Physiochemical properties

Fig. 1 provide representative TEM images and particle sizes distribution of the hydrogenated and hydrogenated following UV-light pre-treated SiO$_2$, TiO$_2$, and 9TiO$_2$–1SiO$_2$ catalysts, labelled as Si-H, Ti-H, 9Ti-1Si-H, Si-H-UV, Ti-H-UV, and 9Ti-1Si-H-UV, respectively. The TEM images of Si-H and Si-H-UV show that the particles were found to be irregular in shape with a size distribution between 10-30 nm. For the Ti-H and Ti-H-UV samples, the particles appeared to become more rounded with a size distribution between 10–40 nm. In the case of 9Ti-1Si-H and 9Ti-1Si-H-UV depicts that highly crystalline spherical TiO$_2$ nanoparticles interspersed with amorphous SiO$_2$. EDX mapping (Fig. 2) confirmed that titanium and oxygen elements are uniformly distributed throughout the TiO$_2$–SiO$_2$ composites. It is also noted that there exists a homogeneous thin amorphous silica layer in between two spherical TiO$_2$ particles favoring the interaction between TiO$_2$ and SiO$_2$.

Fig. 2 also shows that the majority of the TiO$_2$–SiO$_2$ particles are also well-dispersed nanospheres within a lightly compacted aggregate and with a broad particle size distribution from 5 to 40 nm. Larger TiO$_2$-dominant particles were present following UV light pre-treatment (Fig. 2b), with elemental Si being observed on/in those particles as well. High resolution TEM indicates that 9Ti-1Si-H (Fig. 3a) and 9Ti-1Si-H-UV (Fig. 3b) consists of highly crystalline spherical TiO$_2$ interposed with amorphous SiO$_2$. Lattice fringes with *d*-spacing of 0.353 and 0.325 nm are observed which can be attributed to anatase (101) and rutile (110) crystal phase.

Fig. 4a shows the XRD patterns for the hydrogenated samples (Ti-H, Si-H, 9Ti-1Si-H) and are compared with the catalysts after hydrogenation following UV light pre-treatment (Ti-H-UV, Si-H-UV, and 9Ti-1Si-H-UV). The XRD pattern of
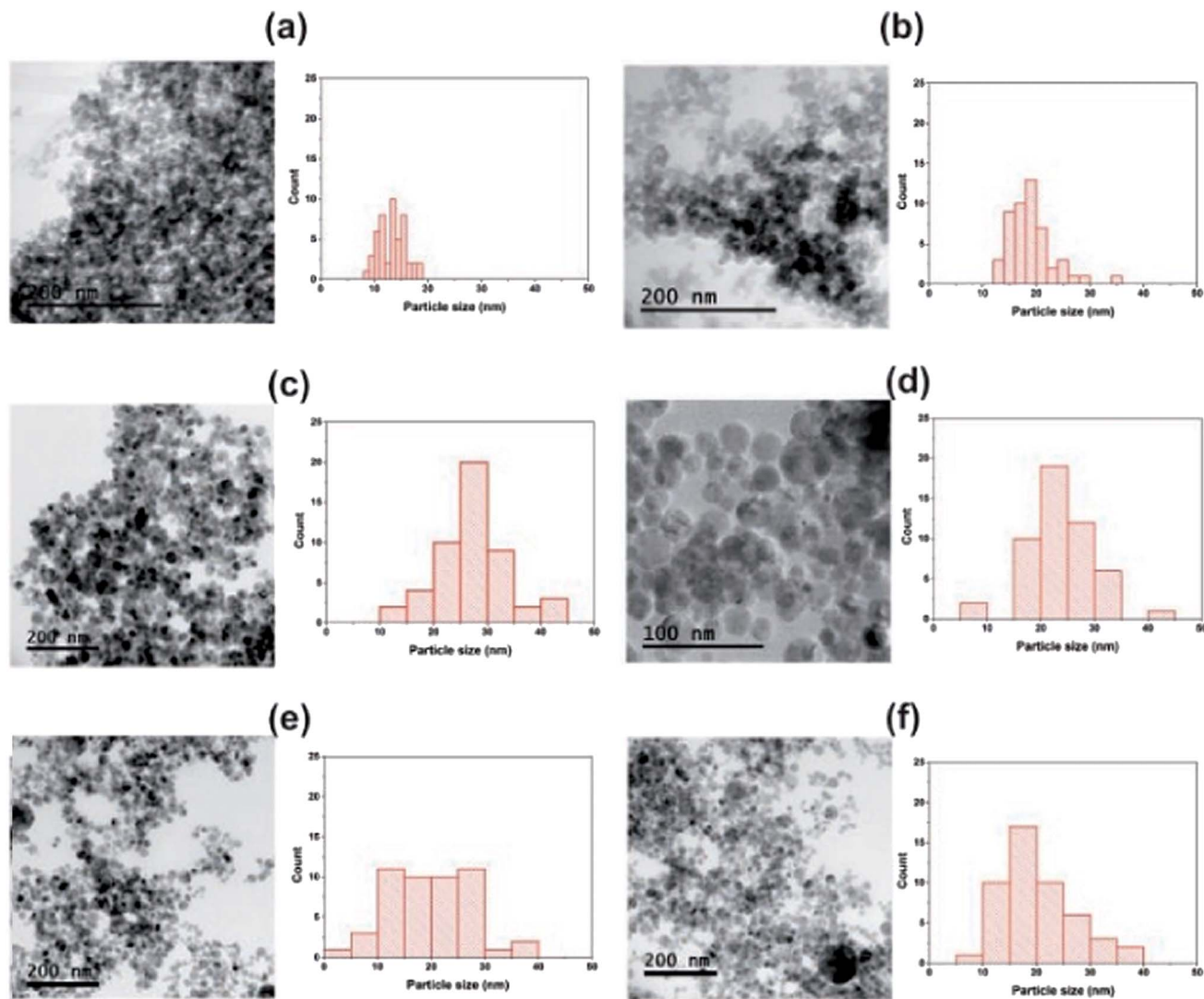
Paper

Fig. 1 TEM images and particle size distributions of (a) Si-H (b) Si-H-UV (c) Ti-H (d) Ti-H-UV (e) 9Ti-1Si-H (f) 9Ti-1Si-H-UV.

hydrogenated TiO_2 samples shows peaks at 25.4°, 37.7°, and 48.1° which are characteristic of the (101), (004), and (200) anatase phase crystal facets (JCPDS 84-1286), while peaks at 27.6°, 36.2°, and 41.5° corresponded to the (110), (101), and (111) rutile phase crystal facets (JCPDS 88-1175). The XRD pattern of the hydrogenated SiO_2 was characterized by a broad peak at 21.5° corresponded to the characteristic of amorphous SiO_2 phase. The diffraction peaks of TiO_2 with a main component of anatase phase and a small fraction of rutile phase can be observed for $9TiO_2$–$1SiO_2$ composites. The XRD patterns provide clear evidence that incorporation of Si atoms into the TiO_2 lattice, suggesting Ti–O–Si bonding is existed. However, there are no significant differences of XRD patterns among all catalysts which were treated without and with UV light pre-treatment.

Fig. 4b provides the UV-vis spectra of the catalysts performed under ambient conditions. The spectra show changes in the light absorption properties of the catalysts, which can be investigated by the existence of a blue color in the $9TiO_2$–$1SiO_2$ composites (Fig. 4b-inset). The parent SiO_2 sample did not display absorption in the UV-vis range as expected given the properties of the insulator materials. The parent TiO_2 sample exhibited an absorption band in the UV range with an onset at about 380 nm, which is a characteristic for a main component of anatase phase crystal structure. In the case of $9TiO_2$–$1SiO_2$ composites, the absorption onset wavelength shifted towards the higher wavelength (blue region). In addition, absorption in the visible region over the 400–650 nm range was clearly observed for the 9Ti-1Si-H and 9Ti-1Si-H-UV samples whereby the intensity of absorption increased as the combination of hydrogenation and UV light pre-treatment were obtained. On the other hand, the broad visible light absorption was not apparent for the neat TiO_2 and neat SiO_2 sample. Visible light absorption of the blue colored TiO_2–SiO_2 composites is corresponded to the formation of Ti^{3+} associated with oxygen vacancy defects.[31] Ti^{3+} species are known to generate mid-gap electronic states within the band gap of TiO_2 and thus lowering the energy band gap of the TiO_2 based catalysts.[32]
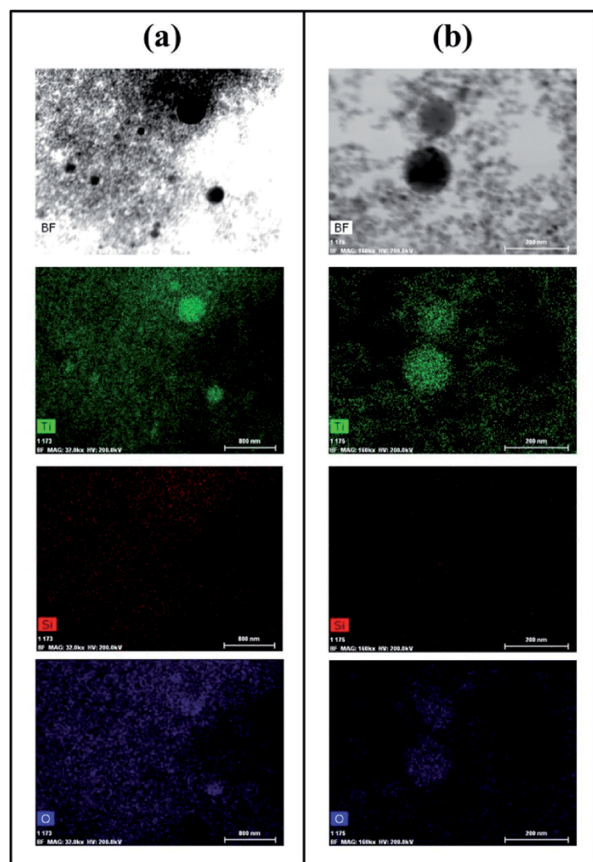
Fig. 2 TEM image, energy dispersive X-ray (EDX) elemental mapping of Ti, Si, and O of (a) 9Ti-1Si-H (b) 9Ti-1Si-H-UV.
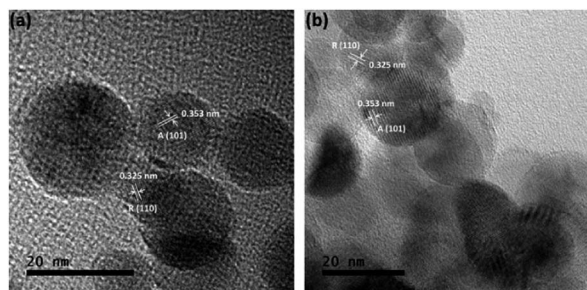

Fig. 3 HRTEM of (a) 9Ti-1Si-H (b) 9Ti-1Si-H-UV.

The existence of defect sites in the hydrogenated SiO_2, TiO_2 and $9TiO_2–1SiO_2$ (Si-H, Ti-H, and 9Ti-1Si-H) and following UV-light pre-treatment (Si-H-UV, Ti-H-UV, and 9Ti-1Si-H-UV) were probed using EPR spectroscopy as shown in Fig. 5a. Based on the EPR results, peaks at g values of 1.952 in the EPR spectra corresponded to the paramagnetic Ti^{3+} centres.[33,34] In addition, the peak at g-value of 2.079 suggests non-bridging oxygen hole centers (NBOHCs) are exist while the peak at g-value of 2.002 indicates oxygen vacancies (Ov) which may coexist with NBOHCs on the hydrogenated SiO_2.[28,35] A g-value signal at 1.952 was observed for neat TiO_2 representing Ti^{3+} centres, although at much lower intensities compared with $9TiO_2–1SiO_2$ as
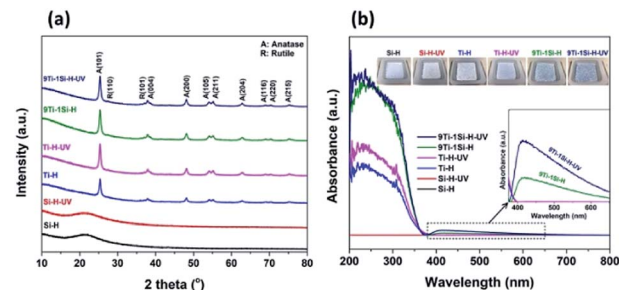

Fig. 4 (a) XRD and (b) UV-vis of Si-H, Si-H-UV, Ti-H, Ti-H-UV, 9Ti-1Si-H, 9Ti-1Si-H-UV. Inset of (b) absorption at the visible light range and the obtained color of catalysts after hydrogenation and hydrogenation following light pre-treatment.

observed from the corresponding double integrated intensity of EPR spectra (Fig. 5b). In some instances, hydrogenated TiO_2 has been reported to generate a weak signal at g value of 2.002, attributed to paramagnetic superoxide species adsorbed on the TiO_2 surfaces which may impose on the oxygen vacancies or NBOHC signals. However, the EPR spectra of hydrogenated TiO_2 give no evidence of a peak at g value 2.002 being present such that it will not interfere with the silica defect signals in the same g-value. The findings demonstrates that a small amount of SiO_2 can assist in stabilizing the Ti^{3+} defect site, reflected in the binary $9TiO_2–1SiO_2$ possessing an enduring blue color (Fig. 4b-inset).

The influence of UV light pre-treatment on defect site formation in the TiO_2, SiO_2 and $9TiO_2–1SiO_2$ composites following hydrogenation treatment was also probed. The EPR spectra (Fig. 5a) and double integrated intensity (Fig. 5b) show that for $9TiO_2–1SiO_2$ there is a distinct escalation of the peak at g-value of 2.079 after UV light pre-treatment, attributed to NBOHC defects. The intensity of the Ti^{3+} defect signal (g = 1.952) and oxygen vacancies (g = 2.002) slightly increased
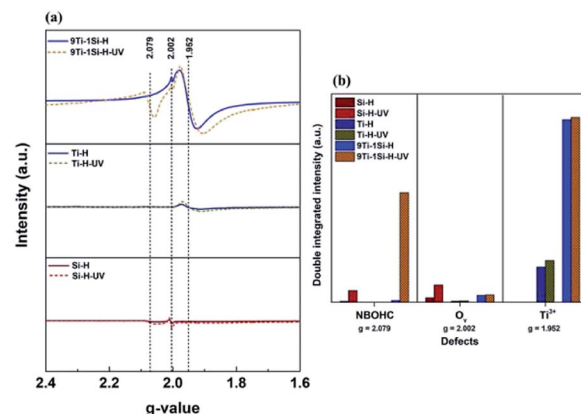

Fig. 5 (a) EPR spectra and (b) double integrated intensity of EPR spectra at g-values of 2.079 (NBOHC), 2.002 (oxygen vacancies, Ov) and 1.952 (Ti^{3+} centers) for hydrogenated SiO_2, TiO_2 and $9TiO_2–1SiO_2$ without UV light pre-treatment (Si-H, Ti-H, and 9Ti-1Si-H) indicated as solid lines, solid bars and following UV light pre-treatment (Si-H-UV, Ti-H-UV, and 9Ti-1Si-H-UV) indicated as dashed lines, cross-hatched bars.

compared with the signal obtained without UV light pre-treatment. NBOHC can be generated by the breaking of strained Si–O–Si linkages or by the rupture of peroxy linkages through hydroxylation.[36] NBOHC can be also generated upon irradiation by oxygen–hydrogen bond breakage from silanol functional groups.[37] The double integrated intensity of the EPR spectra clearly demonstrates that a significant increase in NBOHC defects occurs for $9TiO_2$–$1SiO_2$ composites after UV light pre-treatment, indicating there is an interaction between the TiO_2 and SiO_2 that promotes defect generation.

Fig. 6 shows the deconvoluted XPS spectra at Ti 2p, O 1s and Si 2p core levels. For the Ti 2p core level spectra (Fig. 6a), following UV light pre-treatment of hydrogenated samples, the Ti 2p peaks of $9TiO_2$–$1SiO_2$ shift towards lower binding energy while no significant shift for neat TiO_2. The negative shifts can be attributed to the existence of Ti–O–Si bonds.[38] In addition, Ti^{3+} peaks are observed at binding energy of 457.7 eV (ref. 39) for 9Ti-1Si-H and 9Ti-1Si-H-UV which confirms the EPR results (Fig. 5a). The Si 2p spectra for the hydrogenated SiO_2 and $9TiO_2$–$1SiO_2$ (Fig. 6b) are dominated by a peak centred at a binding energy of 103.0–103.7 eV. This peak is characteristic of Si^{4+} in SiO_2.[28] Following UV light pre-treatment, a negative peak shift was observed, indicating a change in the chemical environment of the Si–O–Si bonds. In the case of the O 1s core level spectra (Fig. 6c), the binding energy for hydrogenated TiO_2 and SiO_2 are in good agreement with the literature relative to O–Ti and O–Si at 530.2 and 533.4 eV, respectively.[40] In the case of the binary $9TiO_2$–$1SiO_2$, the peak shifts towards a negative binding energy following UV light pre-treatment, indicating a higher electron density within the oxygen environment.[41]

Photocatalytic activity assessment

The photocatalytic performance of the hydrogenated TiO_2, SiO_2, and $9TiO_2$–$1SiO_2$ prior to and following UV light pre-treatment was evaluated *via* hydrogen generation in an aqueous mix of water and methanol solutions. Fig. 7 provides the photoactivity profiles under UV-visible-light irradiation (full spectrum), whereby a substantial difference in evolved hydrogen can be observed. Si-H exhibited negligible activity irrespective of the presence of UV light pre-treatment as expected given by the insulating properties of the material. Marginal activity was
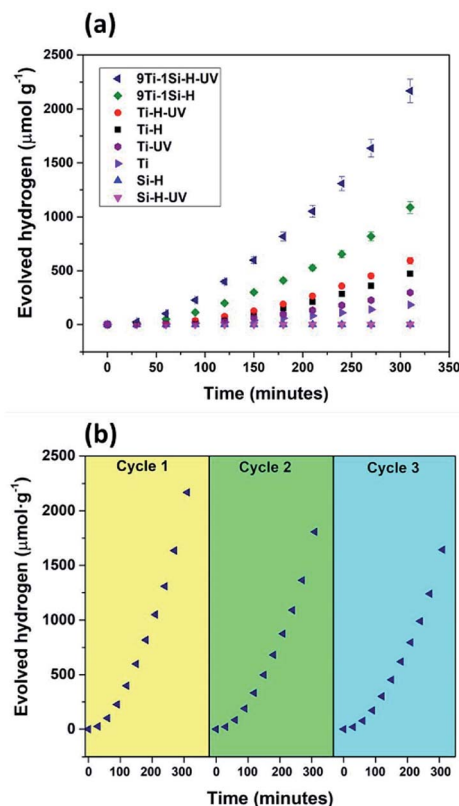
Fig. 6 Deconvoluted XPS spectra of hydrogenated SiO_2, TiO_2 and $9TiO_2$–$1SiO_2$ without UV light pre-treatment (Si-H, Ti-H, and 9Ti-1Si-H) and following UV light pre-treatment (Si-H-UV, Ti-H-UV, and 9Ti-1Si-H-UV) over the (a) Ti 2p (b) Si 2p and (c) O 1s core levels.

Fig. 7 (a) Hydrogen evolution of hydrogenated SiO_2, TiO_2 and $9TiO_2$–$1SiO_2$ without UV light pre-treatment (Si-H, Ti-H, and 9Ti-1Si-H) and following UV light pre-treatment (Si-H-UV, Ti-H-UV, and 9Ti-1Si-H-UV) compared with neat (non-hydrogenated) TiO_2 (Ti) from an aqueous solution including water and methanol under Xenon lamp (full spectrum). (b) Photocatalytic stability test of hydrogen evolution using 9Ti-1Si-H-UV in three cycles. Photocatalyst loading = 50 mg; suspension volume = 150 mL.

displayed by Ti-H and UV light pre-treatment invoked a slight improvement. For 9Ti-1Si-H, the photocatalytic activity was enhanced by two-folds following UV light pre-treatment. The low activity of Si-H may be explained by the insulating properties of SiO_2 materials. In contrast, the efficient charge trapping of defects comprising Ti^{3+}, oxygen vacancies, and NBOHCs in 9Ti-1Si-H and 9Ti-1Si-H-UV (as illustrated by the EPR results, Fig. 5) which promotes an enhancement of photocatalytic activity of water splitting. The variation in performance indicates that the incorporation of small amount of SiO_2 to TiO_2 is advantageous for enhancing its photocatalytic water splitting activity *via* defect formation.

The stability test of the most active catalyst, *e.g.* 9Ti-1Si-H-UV was conducted in three cycles (Fig. 6b). It can be seen that the photoactivity was decreasing gradually by approximately 17% and 24% at second and third cycles, respectively compared to the first cycle. The deactivation of the catalyst can be due to the oxidation of surface oxygen vacancies associated with Ti^{3+} defects[42] and hydrogenation of NBOHC defect.[34]

A schematic depicting photocatalytic water splitting over 9Ti-1Si-U-V has been proposed (Fig. 8), derived from the experimental findings. Initially, as was highlighted by EPR (Fig. 5) and
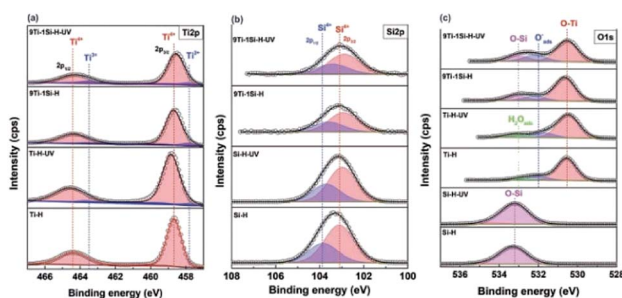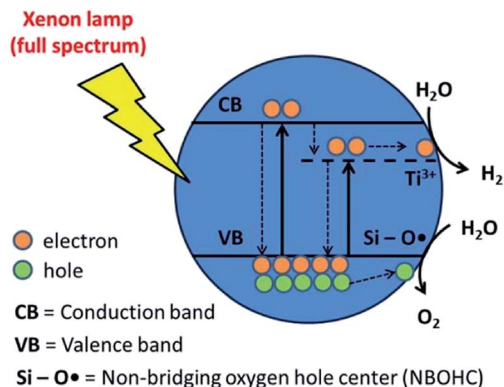
Fig. 8 Schematic mechanism of photocatalytic water splitting on 9Ti-1Si-H-UV in the presence of Ti^{3+} and NBOHC defects.

XPS (Fig. 6), Ti^{3+} species are formed when the Ti–O bond in a Ti–O–Si bridge is broken during the hydrogenation process. Crucially, this leaves a Ti^{3+} site and Si–OH terminal group positioned adjacent to each other. Ti^{3+} may also form by the direct reduction of Ti^{4+} by oxygen extraction or Ti–O–Ti bond breakage; however, given the lower activity of neat TiO_2 compared with TiO_2–SiO_2 composites, this is anticipated to be a secondary process. Upon UV light pre-treatment, a NBOHC defect is generated by dehydroxylation of the Si–OH terminal group adjacent to the Ti^{3+} site. During photocatalytic water splitting process, photogenerated electron was trapped and accumulated by Ti^{3+} and combining with NBOHC defect, it was proposed that both defects were able to facilitate oxidation and reduction of water into oxygen and hydrogen, respectively. This proposed mechanism clearly highlights that catalyst treatments, including hydrogenation and UV light pre-treatment that create multiple defect sites in binary $9TiO_2$–$1SiO_2$ composites, are crucial to the overall photocatalytic water splitting performance.

Conclusions

The presented findings have demonstrated that defect sites can be generated in TiO_2/SiO_2 to invoke a substantial enhancement in photocatalytic water splitting performance. Here, a sequential hydrogenation and UV light pre-treatment approach was employed to produce two distinct and adjacent defect sites in a TiO_2/SiO_2-based material. Hydrogenation generated Ti^{3+} sites while UV light pre-treatment introduced silica-based NBOHC sites. Both defect sites then united to facilitate water splitting reaction more efficiently. The study clearly demonstrates the supremacy of defect engineering and the potential it holds as a versatile approach to upgrade catalyst performance in the ongoing research for low-cost, efficient and abundant catalysts for photocatalytic water splitting processes.

Conflicts of interest

There are no conflicts to declare.

References

1 J. Liu, Y. Liu, N. Liu, Y. Han, X. Zhang, H. Huang, Y. Lifshitz, S.-T. Lee, J. Zhong and Z. Kang, *Science*, 2015, **347**, 970–974.

2 H. Ahmad, S. K. Kamarudin, L. J. Minggu and M. Kassim, *Renewable Sustainable Energy Rev.*, 2015, **43**, 599–610.

3 K. Maeda and K. Domen, *J. Phys. Chem. Lett.*, 2010, **1**, 2655–2661.

4 S. Siahrostami, G.-L. Li, V. Viswanathan and J. K. Nørskov, *J. Phys. Chem. Lett.*, 2017, **8**, 1157–1160.

5 C. Liu, Y. Feng, Z. Han, Y. Sun, X. Wang, Q. Zhang and Z. Zou, *Chin. J. Catal.*, 2021, **42**, 164–174.

6 X. Chen, R. Shi, Q. Chen, Z. Zhang, W. Jiang, Y. Zhu and T. Zhang, *Nano Energy*, 2019, **59**, 644–650.

7 M. Shao, W. Chen, S. Ding, K. H. Lo, X. Zhong, L. Yao, W. F. Ip, B. Xu, X. Wang and H. Pan, *ChemSusChem*, 2019, **12**, 3355–3362.

8 G. Liao, Y. Gong, L. Zhang, H. Gao, G.-J. Yang and B. Fang, *Energy Environ. Sci.*, 2019, **12**, 2080–2147.

9 A. Xu, W. Tu, S. Shen, Z. Lin, N. Gao and W. Zhong, *Appl. Surf. Sci.*, 2020, **528**, 146949.

10 C. Martinez Suarez, S. Hernández and N. Russo, *Appl. Catal., A*, 2015, **504**, 158–170.

11 S.-H. Chen, Y.-S. Jiang and H.-y. Lin, *ACS Omega*, 2020, **5**, 8927–8933.

12 W. Zhong, W. Tu, Z. Wang, Z. Lin, A. Xu, X. Ye, D. Chen and B. Xiao, *J. Energy Chem.*, 2020, **51**, 280–284.

13 G. Liao, J. Fang, Q. Li, S. Li, Z. Xu and B. Fang, *Nanoscale*, 2019, **11**, 7062–7096.

14 C. Liu, Q. Zhang, W. Hou and Z. Zou, *Sol. RRL*, 2020, 2000070.

15 J. Tang, J. R. Durrant and D. R. Klug, *J. Am. Chem. Soc.*, 2008, **130**, 13885–13891.

16 A. Yamakata, T.-a. Ishibashi and H. Onishi, *J. Mol. Catal. A: Chem.*, 2003, **199**, 85–94.

17 K. Reilly, B. Fang, F. Taghipour and D. P. Wilkinson, *J. Catal.*, 2017, **353**, 63–73.

18 M. Ni, M. K. H. Leung, D. Y. C. Leung and K. Sumathy, *Renewable Sustainable Energy Rev.*, 2007, **11**, 401–425.

19 A. Miyoshi, S. Nishioka and K. Maeda, *Chem. - Eur. J.*, 2018, **24**, 18204–18219.

20 K. Afroz, M. Moniruddin, N. Bakranov, S. Kudaibergenov and N. Nuraje, *J. Mater. Chem. A*, 2018, **6**, 21696–21718.

21 Z. Wang, C. Li and K. Domen, *Chem. Soc. Rev.*, 2019, **48**, 2109–2125.

22 Y.-C. Zhang, N. Afzal, L. Pan, X. Zhang and J.-J. Zou, *Adv. Sci.*, 2019, **6**, 1900053.

23 T. Takata and K. Domen, *J. Phys. Chem. C*, 2009, **113**, 19386–19388.

24 M. S. Hamdy, W. H. Saputera, E. J. Groenen and G. Mul, *J. Catal.*, 2014, **310**, 75–83.

25 Z. Zheng, B. Huang, J. Lu, Z. Wang, X. Qin, X. Zhang, Y. Dai and M.-H. Whangbo, *Chem. Commun.*, 2012, **48**, 5733–5735.

26 Y. H. Hu, *Angew. Chem., Int. Ed.*, 2012, **51**, 12410–12412.

27 W. H. Saputera, G. Mul and M. S. Hamdy, *Catal. Today*, 2015, **246**, 60–66.

28 W. H. Saputera, H. A. Tahini, E. C. Lovell, T. H. Tan, A. Rawal, K.-F. Aguey-Zinsou, D. Friedmann, S. C. Smith, R. Amal and J. Scott, *J. Catal.*, 2019, **376**, 168–179.

29 W. H. Saputera, H. A. Tahini, M. Sabsabi, T. H. Tan, N. M. Bedford, E. Lovell, Y. Cui, J. N. Hart, D. Friedmann, S. C. Smith, R. Amal and J. Scott, *ACS Catal.*, 2019, **9**, 2674–2684.

30 W. H. Saputera, J. Scott, H. Tahini, G. K. C. Low, X. Tan, S. Smith, D.-W. Wang and R. Amal, *ACS Catal.*, 2017, **7**, 3644–3653.

31 G. Zhu, Y. Shan, T. Lin, W. Zhao, J. Xu, Z. Tian, H. Zhang, C. Zheng and F. Huang, *Nanoscale*, 2016, **8**, 4705–4712.

32 G. Yin, X. Huang, T. Chen, W. Zhao, Q. Bi, J. Xu, Y. Han and F. Huang, *ACS Catal.*, 2018, **8**, 1009–1017.

33 R. F. Howe and M. Gratzel, *J. Phys. Chem.*, 1985, **89**, 4495–4499.

34 W. H. Saputera, H. A. Tahini, M. Sabsabi, T. H. Tan, N. M. Bedford, E. Lovell, Y. Cui, J. N. Hart, D. Friedmann, S. C. Smith, R. Amal and J. Scott, *ACS Catal.*, 2019, 2674–2684, DOI: 10.1021/acscatal.8b04891.

35 M. Stapelbroek, D. L. Griscom, E. J. Friebele and G. H. Sigel, *J. Non-Cryst. Solids*, 1979, **32**, 313–326.

36 H. Nishikawa, R. Nakamura, R. Tohmon, Y. Ohki, Y. Sakurai, K. Nagasawa and Y. Hama, *Phys. Rev. B*, 1990, **41**, 7828–7834.

37 L. Skuja, *J. Non-Cryst. Solids*, 1998, **239**, 16–48.

38 R. P. Netterfield, P. J. Martin, C. G. Pacey, W. G. Sainty, D. R. McKenzie and G. Auchterlonie, *J. Appl. Phys.*, 1989, **66**, 1805–1809.

39 L.-B. Xiong, J.-L. Li, B. Yang and Y. Yu, *J. Nanomater.*, 2012, **2012**, 13.

40 G. M. Ingo, S. Dirè and F. Babonneau, *Appl. Surf. Sci.*, 1993, **70–71**, 230–234.

41 W. H. Saputera, J. A. Scott, D. Friedmann and R. Amal, *Appl. Catal., B*, 2018, **223**, 216–227.

42 S. Mohajernia, P. Andryskova, G. Zoppellaro, S. Hejazi, S. Kment, R. Zboril, J. Schmidt and P. Schmuki, *J. Mater. Chem. A*, 2020, **8**, 1432–1442.